Journal of Chromatography A, 1218 (2011) 3466–3475

Contents lists available at ScienceDirect

Journal of Chromatography A

journal homepage: www.elsevier.com/locate/chroma

Modeling of flow in a polymeric chromatographic monolith

Harun Koku[a], Robert S. Maier[b], Kirk J. Czymmek[c], Mark R. Schure[d], Abraham M. Lenhoff[a,*]

[a] Department of Chemical Engineering, University of Delaware, Newark, DE 19716, USA
[b] Information Technology Laboratory, USA Army Engineer Research and Development Center, Vicksburg, MS 39180, USA
[c] Department of Biological Sciences, University of Delaware, Newark, DE 19716, USA
[d] Theoretical Separation Science Laboratory, The Dow Chemical Company, 727 Norristown Road, Spring House, PA 19477-0904, USA

ARTICLE INFO

Article history:
Received 7 December 2010
Received in revised form 22 March 2011
Accepted 28 March 2011
Available online 4 April 2011

Keywords:
Monolith
CIM disk
Scanning electron microscopy
Lattice-Boltzmann
Simulation
Flow field
Permeability

ABSTRACT

The flow behavior of a commercial polymeric monolith was investigated by direct numerical simulations employing the lattice-Boltzmann (LB) methodology. An explicit structural representation of the monolith was obtained by serial sectioning of a portion of the monolith and imaging by scanning electron microscopy. After image processing, the three-dimensional structure of a sample block with dimensions of 17.8 μm × 17.8 μm × 14.1 μm was obtained, with uniform 18.5 nm voxel size. Flow was simulated on this reconstructed block using the LB method to obtain the velocity distribution, and in turn macroscopic flow properties such as the permeability and the average velocity. The computed axial velocity distribution exhibits a sharp peak with an exponentially decaying tail. Analysis of the local components of the flow field suggests that flow is not evenly distributed throughout the sample geometry, as is also seen in geometries that exhibit preferential flow paths, such as sphere pack arrays with defects. A significant fraction of negative axial velocities are observed; the largest of these are due to flow along horizontal pores that are also slightly oriented in the negative axial direction. Possible implications for mass transfer are discussed.

1. Introduction

In preparative chromatography of large molecules in traditional packed columns, mass transfer phenomena are usually rate-limiting [1] due to low diffusivities of higher molecular weight solutes [2]. One way to circumvent such diffusional limitations is to maximize the contribution of convective transport [3–5]. This idea has led to the development of monolithic materials for chromatography – continuous blocks of solid with large through-pores that enable uninterrupted bulk flow. Methods of synthesis, physical and chemical properties and practical applications of these materials are now well documented [6–9].

Monoliths can be classified into silica-based monoliths [10,11] and organic polymer-based monoliths [12,13] with respect to their base material, and this distinction is reflected in their significantly different morphologies. Silica monoliths are typically networks of interconnected, rod-like structures and have a sharp bimodal pore size distribution with large through-pores between the rods and smaller mesopores on the rods themselves [14,15]. In polymeric monoliths, on the other hand, although control of global porosity is possible through careful formulation and synthesis [8,9,16,17], the resulting structures are much more heterogeneous (Fig. 1), with pore size distributions spanning several orders of magnitude [18–20]. In terms of applications, silica-based monoliths are typically preferred for separation of low molecular weight molecules such as polypeptides and aromatic compounds, while polymeric monoliths have generally been used for purification of larger bioparticles such as antibodies [21], viruses [22–24] and plasmid DNA [25,26].

Numerous studies have evaluated the performance of monoliths, in particular the extent to which they fulfill the expectations of enhanced permeability and efficiency due to their larger pore sizes and convective transport. For both silica and polymeric monoliths, the Darcy equation,

$$\frac{\Delta P}{L} = \frac{\mu u_s}{\kappa} \tag{1}$$

in which the pressure drop per unit length of column $\Delta P/L$ is a linear function of the mobile phase superficial velocity u_s, captures the experimentally observed trends between velocity and pressure drop well [7,27–30]. Here μ is the dynamic viscosity and κ the permeability. The absolute permeabilities of the commercial Chromasil™ silica monoliths are on the order of 0.01 μm^2 and in general several-fold higher than those of packed columns with similar separation efficiency [6]. For polymeric monoliths, on the other hand, the value of the permeability may vary broadly depending on different formulations for synthesis [16]. Absolute permeabilities of

* Corresponding author. Tel.: +1 302 831 8989; fax: +1 302 831 1048.
E-mail address: lenhoff@udel.edu (A.M. Lenhoff).

0021-9673/$ – see front matter © 2011 Elsevier B.V. All rights reserved.
doi:10.1016/j.chroma.2011.03.064

Fig. 1. An SEM image of the BIA Separations CIM disk monolith.

0.004–0.01 μm^2 have been reported for the commercial CIM^{TM} disk monoliths [18,27,31].

The most common measure of separation efficiency is peak broadening, or the height equivalent to a theoretical plate (HETP), which is considered to be the combined result of axial or lateral molecular diffusion in the mobile phase, dispersion due to flow patterns, and solute transport-adsorption phenomena at the solid–liquid interface [32–35]. Studies on silica monoliths reveal HETP curves flatter than those for packed particles [36–38], suggesting comparatively lower mass transfer resistance and indicating that the band-spreading is dominated by axial diffusion–dispersion at low to moderate flow rates [39–41]. Steeper HETP curves at high flow rates are observed when high molecular weight compounds are employed, however, possibly due to slower mass transfer kinetics in the mesopores [38]. Studies on polymeric monoliths are comparatively fewer, but the diminished role of mass transfer appears evident from studies with methacrylic CIM disks where the HETP value is observed to be virtually independent of mobile phase velocity, indicating that peak broadening is mainly due to axial dispersion and extra-column effects [7,21,42–44].

These studies have been successful in experimentally characterizing and comparing the performance of monolithic materials. However, bridging the gap between correlations that correspond to the macroscopic behavior and the underlying flow and mass transfer phenomena requires theoretically correct representations of the systems studied, often at the microscopic scale [35,45–47]. For example, while the Darcy equation (Eq. (1)) is an adequate representation of the pressure drop behavior, attempts to relate permeabilities to structural parameters such as porosity or an estimated equivalent particle size are not always satisfactory [27,48], as they are often based on correlations like the Kozeny–Carman equation, which were originally derived for packed beds. Likewise, despite strong indications of the considerable role of mechanical dispersion in the overall HETP of monoliths, the axial dispersion is generally lumped into a single dispersion coefficient, again based on an equivalent particle size.

Therefore, a more rigorous mechanistic analysis of the complex interaction of the flow field with the monolith geometry should include some description of the actual pore structure, and previous research to this end varies with respect to the level of resolution of the topography. For example, Meyers and Liapis extended their pore network modeling efforts to the silica monolith geometry by reducing it to a cubic lattice network of pores [49,50]. Miyabe and coworkers applied their general rate model theory to silica monoliths using a simplified representative geometry with a unit skeleton [41,51] to obtain exact expressions for the plate height and coupled their results to experimental moment profiles to estimate the remaining unknown parameters. Desmet and coworkers [48,52–54] implemented a similar approach, by generating a simplified three-dimensional model that mimics the silica monolith skeleton through replication of a symmetric tetrahedral cell, and computing the flow and dispersion characteristics for this geometry. Differences between the calculated results for the simplified structure and the experimentally observed behavior of silica monoliths were attributed to the heterogeneity of real systems, which is not captured by uniform geometry of the model [48,54].

In contrast to these studies, where the geometry is reduced to a representative structure, methods in which the structure is represented at its smallest descriptive level with no adjustable parameters have been gaining traction, thanks to advances in both imaging methods and the capabilities of computational hardware and software. The power of this approach has previously been demonstrated for simulation of packed beds of spheres where, in addition to obtaining results that correctly reproduced experimental behavior, it has been possible to implement very detailed studies of the underlying transport phenomena, such as extracting the directional components of dispersion, elucidating the influence of structural parameters like packing order and homogeneity, defects, column walls and duct shape, and analysis of the time and length scales involved in flow and dispersion [55–69]. Recently Hlushkou et al. have demonstrated this methodology for silica monoliths, implementing a complete pore-scale solution of the velocity distribution to obtain the flow characteristics [70] and in turn the dispersion behavior [71] from a reconstructed sample of silica monolith. Their flow results show excellent agreement with experimental permeability data, whereas the dispersion simulations yield lower plate heights compared to experimental column behavior, which the authors attribute to the absence of wall effects [71].

As mentioned previously, polymeric monoliths exhibit a broader size distribution and much greater heterogeneity than silica monoliths. Hence a pore scale solution of the flow field and dispersion based on a direct representation of the stationary phase is not only useful in achieving a greater depth of analysis, but also somewhat inevitable due to the inherent difficulty of introducing a reduced geometry that is able to mimic the topography of the real system. In this study we analyze the flow behavior in a commercial polymeric monolith, the CIM^{TM} (convective interaction media) disk from BIA Separations, by implementing a direct numerical simulation of flow in a three-dimensional (3D) sample reconstructed from high resolution scanning electron microscopy (SEM) images of serial sections. To our knowledge, this is the first time the explicit flow-field analysis of polymeric monoliths has been implemented in this manner. The velocity map for the CIM monolith was obtained using lattice-Boltzmann (LB) methodology [72–74]. This class of methods is well suited for simulations of flow in irregular geometries at low Reynolds numbers. It has previously been used to obtain flow fields in complex pore structures of diverse materials such as sandstone [75], a silicon carbide matrix [76] and asphalt [77]. LB simulations of sphere packs have been used to model flow and dispersion in non-porous [57–63,67–69] and porous [64,65] beads, and the results have been shown to be in good agreement with experimental velocity fields observed using NMR velocimetry [78].

2. Methods

2.1. Scanning electron microscopy imaging

Structural data were acquired by backscatter SEM, which uses sample preparation procedures almost identical to those for transmission electron microscopy (TEM). Therefore standard protocols [79] for preparation of biological specimens for TEM imaging were followed in preparing the monolith samples. About 1–2 mm

thick pieces of a CIM DEAE anion-exchanger monolith disk (BIA Separations, batch number 05-GE01-012-001B) were allowed to equilibrate with 5 g/L α-lactalbumin (Sigma, purity ≥ 85%, lot no. 035K7005) in a 20 mM, pH 8.0 phosphate buffer solution. The samples were chemically fixed by 1% paraformaldehyde and 1% glutaraldehyde in 50 mM phosphate buffer solution, rinsed in deionized water and post-fixed in 1% osmium tetroxide in deionized water. Samples were then rinsed and dehydrated in a graded series of glass-distilled acetone, infiltrated with Embed 812, poured into molds and cured in an oven thermostated at 65 °C for 3 days. All chemicals used for fixing, staining and embedding the samples were purchased from Electron Microscopy Sciences.

Automated serial-sectioning and backscatter imaging of the samples were performed by Gatan Instruments, Inc., in a variable-pressure field emission SEM equipped with a Gatan 3-View system [80]. A total of 281 serial sections, each 50 nm thick, were obtained.

2.2. Image processing

All image processing was carried out using Matlab (Mathworks, Inc) and NIH ImageJ software. The backscatter image data were smoothed by anisotropic diffusion [81] to filter out noise and to enhance edge definition (Fig. 2b), then binarized (converted to black and white, Fig. 2c) by automated Otsu thresholding [82].

The LB method used in this work utilizes a cubic grid with isotropic voxels, whereas due to the nature of the sectioning-imaging procedure, our original data set had unequal voxel dimensions of 18.5 nm per pixel for the face and 50 nm for the thickness of each section. Using grey-scale value interpolation, intermediate slices were synthesized in order to achieve isotropic voxel dimensions of 18.5 nm in all three dimensions. This was done by calculating the positions of the slices to be synthesized, and obtaining them by linear interpolation between the closest sections above and below.

The flow simulations employ periodic boundary conditions, but since features at one end of the block are very unlikely to fuse smoothly to the topography at the other end, this procedure introduces jump discontinuities with concomitant distortion of the flow field calculations at edges. For this reason, a final alteration to the geometry that was implemented to ensure continuity in the simulations was a mirroring algorithm, in which the ends of the block were treated as symmetry faces to 'reflect' the features.

The porosity and pore size distribution (PSD) of the reconstructed block were calculated by image analysis, through application of concepts in mathematical morphology [83]. Briefly, the image was subjected to successive erosion and dilation steps using a 'structuring element' or probe of a selected size. The fraction of void pixels, that is, the apparent porosity of the resulting image, corresponds to the point for the same probe size on an inverse cumulative PSD curve. Specific details of the procedure are available elsewhere [84,85].

2.3. Flow simulation

The LB simulation is based on a lattice representation of the discrete-velocity Boltzmann transport equation. The monolith geometry was mapped to the lattice by assigning lattice nodes at the center of each image voxel. In this spatial lattice, fluid velocity is also a discretized quantity, defined as a preset number of velocity vectors in different directions. The number of these vectors depends on the specific two- or three-dimensional LB model adopted, and their length and direction correspond to the distance and orientation between neighboring lattice nodes. Each fluid node has an associated set of mass distribution functions f_i, and it is the interaction of these functions among the nodes and along the velocity vectors, together with a collision model within each node, that forms the basis of the flow. Specifically, local densities and momenta are defined for each node through the mass distribution function

$$\rho = \sum_{i=1}^{q} f_i, \quad i = 1, \ldots, q$$
$$\rho \mathbf{v} = \sum_{i=1}^{q} f_i e_i, \quad i = 1, \ldots, q \tag{2}$$

Here, ρ is the local fluid density, ρv is the local momentum and q is the total number of velocity vectors associated with the lattice model. e_i and f_i are the unit velocity vectors and the distribution functions, respectively (the mapping of these lattice quantities to physical units is described below).

The local mass and momentum are updated iteratively through the mass distribution functions by a combination of inter-node streaming and relaxation to the Maxwell–Boltzmann equilibrium within each node:

$$f_i(r + e_i, t+1) = f_i(r,t) - \frac{1}{\omega}[f_i(r,t) - f_i^{\mathrm{eq}}(\rho, \mathbf{v})] + F(r) \cdot e_i, \quad i = 1, \ldots, q \tag{3}$$

Here the position vector r indicates the lattice node, so the term on the left-hand side is the mass distribution function of the node that neighbors the node denoted by the first term on the right-hand side of the equation, along the direction of the individual velocity vector e_i, at the updating time. The second term on the right-hand side accounts for collision between fictitious lattice particles, with ω as the relaxation time and f_i^{eq} as the equilibrium distribution function; this is known as the Bhatnagar–Gross–Krook (BGK) approximation to the collision operator. The equilibrium distribution function is given by:

$$f_i^{\mathrm{eq}}(\rho, v) = \rho[A_i + B_i e_i \cdot \mathbf{v} + C_i (e_i \cdot \mathbf{v})^2 + D_i \mathbf{v}.\mathbf{v}], \quad i = 1, \ldots, q \tag{4}$$

The coefficients in Eq. (4) are chosen so as to recover the Navier–Stokes equation in the low Mach number limit [86] and their values depend on the lattice model selected. The last term in Eq. (3) corresponds to an arbitrary body force that is imposed at every iteration.

Solid boundaries have to be dealt with separately, since the mass distribution functions *from* the solid nodes to the fluid are undefined. Typically, the unknown distribution functions are obtained by substituting the fluid f_i values in the opposite direction (i.e., heading *to* the solid node) into the unknown ones:

$$f_i(r + e_i, t+1) = f_j(r + e_i, t+1), \quad \text{where } e_j = -e_i \tag{5}$$

This treatment is referred to as the bounce-back boundary condition.

In this work, the lattice model used was d3q19, which indicates a cubic lattice in three dimensions with 19 velocity vectors (i.e. $q = 19$ in Eqs. (3)–(5)). In this model, the lattice kinematic viscosity and equation of state are defined as $\nu = (2\omega - 1)/6$ and $p = c^2\rho$, where p is the lattice pressure and $c^2 = 1/3$ is the square of the lattice sound speed.

Lattice quantities are mapped to physical units through the appropriate discretization parameters. The spatial discretization parameter Δx is the physical distance corresponding to the node spacing, i.e., unit distance on the lattice. The temporal discretization parameter Δt is the physical time step corresponding to one iteration of Eq. (3). Δm is the physical mass corresponding to unit mass on the lattice. For example, the physical velocity u corresponding to a given lattice velocity is $u = \mathbf{v} \cdot \Delta x/\Delta t$.

In the present work, we set Δx equal to 18.5 nm, the sample voxel dimension, and the relaxation parameter $\omega = 1$, and hence $\nu = 1/6$. The values of Δt and Δm follow as 5.70×10^{-11} s and

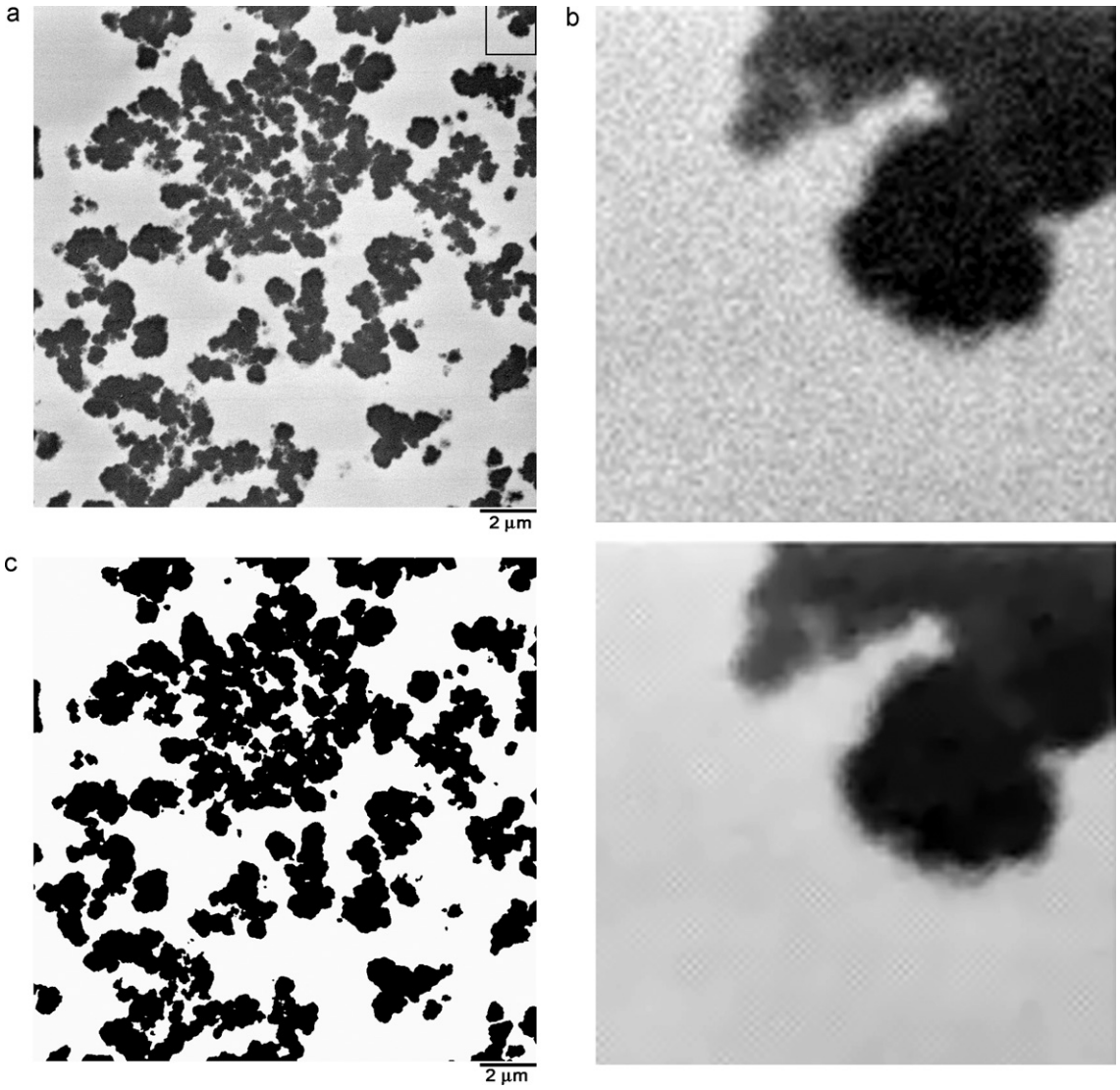

Fig. 2. (a) A raw section obtained by backscatter SEM. The frame at top right indicates region that is magnified. (b) Detail of the framed region in (a), before (top) and after (bottom) application of the noise filter. (c) Final image after binarization by Otsu thresholding.

6.33×10^{-21} kg, respectively, by assuming the fluid to be water with a kinematic viscosity of 1.0×10^{-6} m^2/s = $\nu\,(\Delta x)^2/\Delta t$.

Initial conditions for the flow simulation were unit density and zero velocity everywhere on the lattice. A body force was used to drive the flow [57,87]. The forcing vector, F, was taken as uniform over the lattice, with zero components in the transverse (x, y) directions and a positive component in the axial (z) direction. Periodic boundary conditions were imposed on the external boundaries of the rectangular flow domain in all three dimensions, as mentioned in Section 2.2 and illustrated in Section 3.1. The uniformly imposed forcing term has an effect that is equivalent to a uniform pressure gradient in the axial direction. Using the present lattice model, $\partial p/\partial z = 10\ F_z\ \Delta m/((\Delta x)^2(\Delta t)^2)$, where F_z is the non-zero axial component of the forcing vector.

The lattice Boltzmann iteration (3)–(5) solves the pseudo-transient problem towards a steady-state solution. The iteration is considered to have converged when the relative change in mean pore velocity $\bar{u} = u_z^{\text{avg}}$, given later by equation (6), is small, i.e., $(\bar{u}^{t+10} - \bar{u}^t) < 10^{-4}\,(\bar{u}^{t+10} + \bar{u}^t)/2$, where $\bar{u}^{t+10}$ denotes the mean velocity at iteration number $t + 10$.

The flow simulation was implemented in Fortran 77 for a distributed-memory computer architecture, using the MPI communication library [88]. The simulations were run on a Cray XT3 system located at the U.S. Army Engineer Research and Development Center in Vicksburg, MS. A typical simulation used 2048 AMD Opteron (2.6 GHz) processor cores and required approximately ten thousand iterations and four hours (wall time) for convergence.

3. Results and discussion

3.1. Sample structure

A stack of 281 sections was obtained by automated serial sectioning, with a thickness of 50 nm per section. The resulting stack had dimensions of 17.8 μm × 17.8 μm (962 × 962 voxels) along the face of a section and 14.1 μm as the total thickness. One section (number 149) showed significant folding damage and was replaced by one obtained by interpolation of the sections immediately above and below. Fig. 3 displays a 3D rendering of the reconstructed block, which does not seem to have apparent bias in any direction; thus the choice of the flow direction was arbitrary, implying an assumption of isotropy that is also supported by experimental bulk characterization of these materials [8,89,90]. The direction along the thickness of the individual sections was designated as the flow

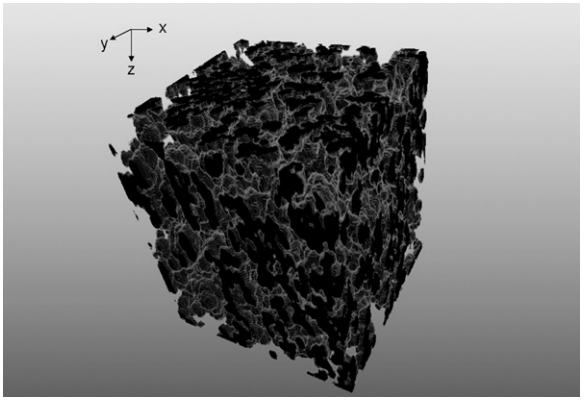

Fig. 3. A rendering of the reconstructed monolith structure before mirroring (the 'raw' structure). Black indicates solid.

direction in simulations (via application of the pressure gradient), thus becoming the axial dimension, *z*. Accordingly, the remaining directions along the faces of the individual sections became the lateral dimensions in the flow simulation, designated *x* and *y*. This block is referred to as the 'raw' structure henceforth.

Because of the mirroring procedure that was applied to the raw geometry, the final structure used in the simulations, designated the mirrored geometry henceforth, had dimensions of 35.6 μm × 35.6 μm × 27.9 μm (1922 × 1922 × 1510 voxels) with a uniform voxel length of 18.5 nm. Fig. 4 displays the first section of the block mirrored in two dimensions and depicts the size of the final three-dimensional mirrored geometry used for the simulations.

3.2. Porosity and pore size distribution (PSD)

The global porosity of the mirrored structure was estimated from image analysis to be 0.57, which is close to the experimental value of 0.55 from non-retained pulse data of small molecules [18]. Similarly, the PSD of the raw sample block obtained from image analysis matched previously reported trends in studies where a similar methodology was implemented for the same type of material [18,19]. On the other hand, the PSD acquired in this manner does not match results from mercury intrusion porosimety, as has been noted previously [18,19]. As discussed in detail elsewhere [18], the discrepancy could be due to limitations of the mercury intrusion process, or inadequate sampling of the monolith in PSD determination by image processing, although the observation of similar PSD characteristics for the CIM monolith in two unrelated studies using two different image processing methods suggests that the distinction is reproducible and not merely a sampling issue.

It is of interest to determine the effect, if any, of the mirroring procedure on the pore size distribution, which is one measure of the microstructure that should be reproduced. Intuitively, these two distributions would be expected to be identical since the mirrored structure is simply a replication of the raw block. However, this argument assumes that the formation of new topographical features at the central regions, brought about by the mirroring process, has no impact on the overall PSD.

The assumption was tested by comparison of the two-dimensional PSDs of the mirrored and raw structures using isolated regions in sample sets of 15 sections selected to span the entire length of each block (Fig. 5a). It can be seen in Fig. 5b that the PSD of the mirrored structure is very similar to that of the raw structure, as expected. The average pore sizes show a very slight difference: 1.27 μm for the raw structure vs. 1.31 μm for the mirrored one. On the other hand, when the region encompassing the intersection of the mirroring axes (Region III in Fig. 5a) is isolated and analyzed

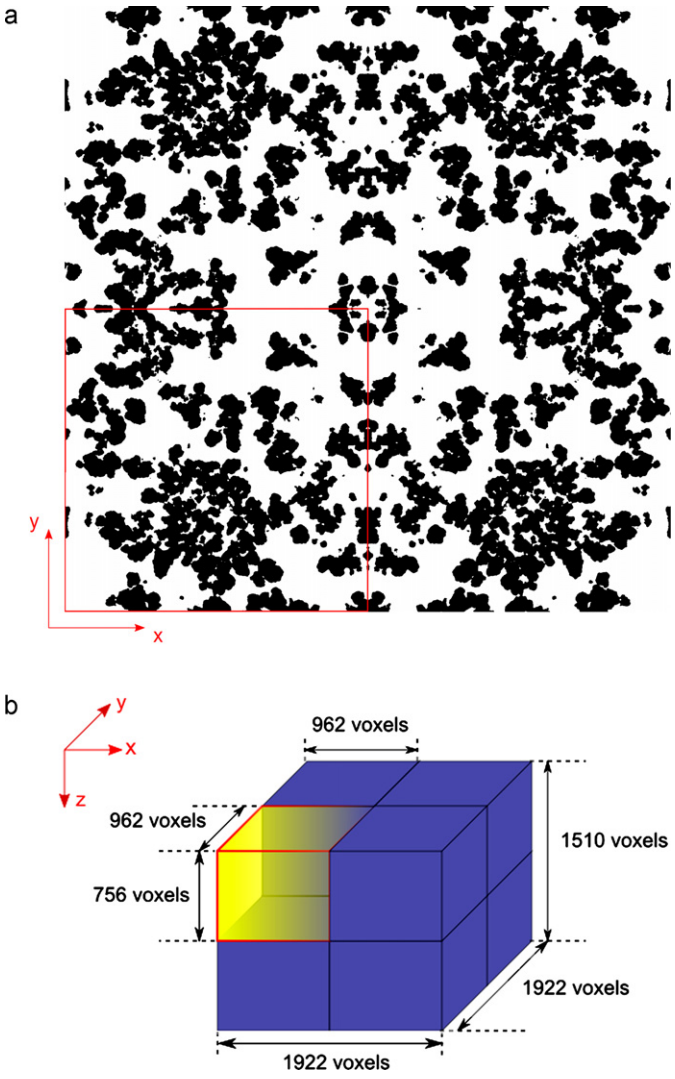

Fig. 4. (a) Illustration of the mirroring procedure in two dimensions. The framed picture is an original section. Black regions designate the solid material; white regions are void. (b) Dimensions of the final mirrored geometry. The light-colored box illustrates the dimensions of the original sample block.

separately, its PSD does seem to exhibit significant distortion, especially towards the higher end of pore size (Fig. 5c), even though its average pore size of 1.33 μm is still close to that of the raw structure. One possible explanation is that pores that have one or more of the symmetry axes as an edge fuse with their mirrored counterparts across the symmetry axes, generating larger pores at the expense of the original pore sizes. For instance, close examination of Fig. 5c reveals that compared to the raw section, the fraction of pores with sizes between 0.75 and 1.25 μm is significantly lower, whereas the fraction of pores sized approximately 2.0 μm marks a sharp peak that is absent in the raw section PSDs. Based on the explanation above, this could be interpreted as resulting from fusion of pores of approximately 1.0 μm diameter with their mirror images. Such behavior is not observed at lower pore sizes, where the mirrored and raw PSDs overlap, presumably because smaller pores are more likely to be completely buried within solid regions rather than being exposed on a symmetry axis. Regardless of the underlying cause, it is possible that this apparent distortion of the PSD in the central region affects the flow field, as is discussed in the corresponding sections.

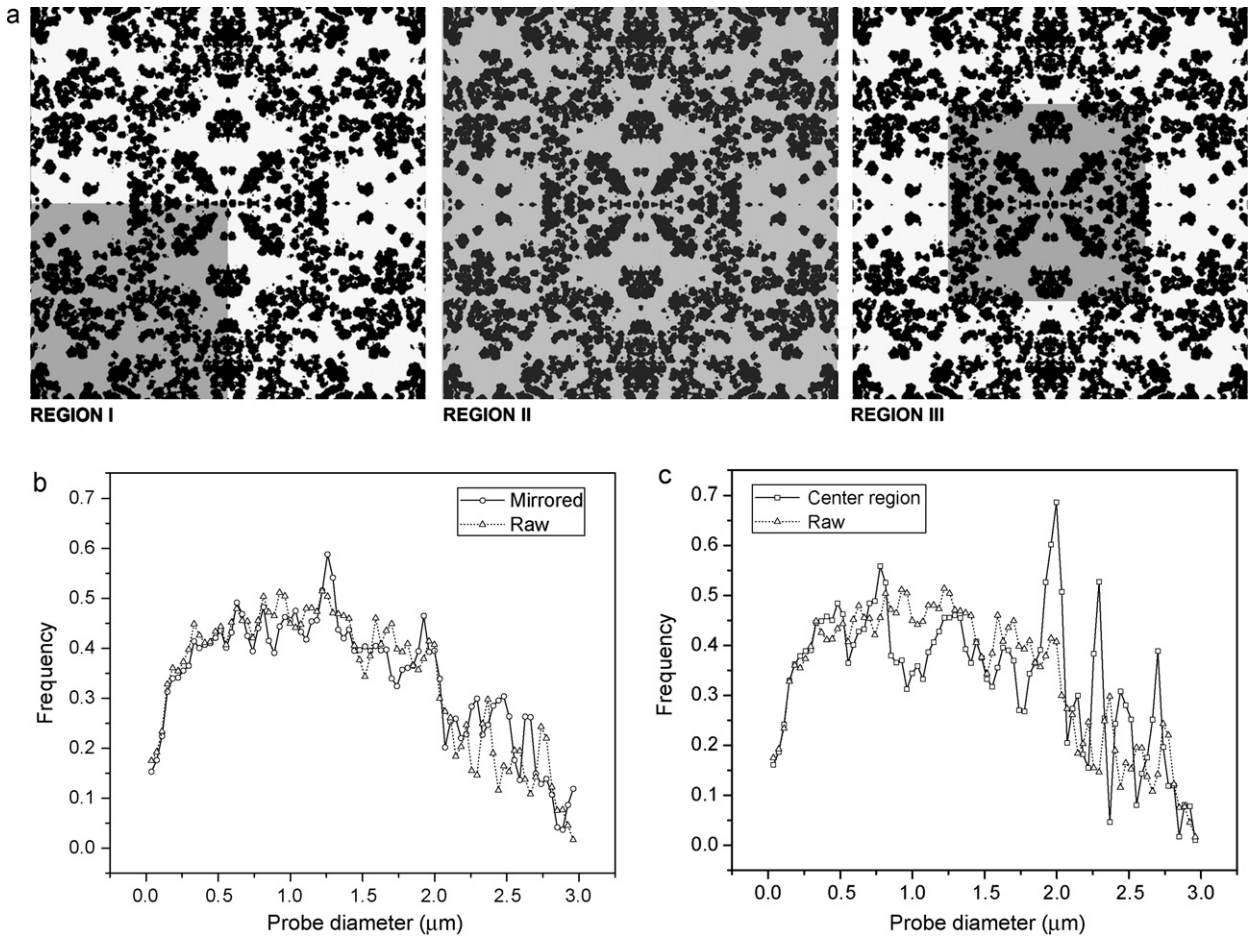

Fig. 5. (a) Regions utilized in PSD comparison of raw and mirrored structures. Region I is the raw section and corresponds to the bottom-left quadrant of the mirrored section. Region II corresponds to the entire mirrored section, while Region III is a raw-section sized image centered on the symmetry point of the mirrored section. (b) Comparison of the raw section image PSD (region I, triangles) to the averaged mirrored section image PSD (region II, circles). Frequencies have been normalized to form PSD curves of unit integral. (c) Comparison of the raw section image PSD (region I, triangles) to the central image PSD (region III, squares).

3.3. Flow field

3.3.1. Average velocity and permeability

In the base case of our simulations, the flow of water was modeled through the mirrored structure driven by a preset pressure drop of 1.59 kPa along the z-direction. This corresponds to a pressure drop for a whole CIM disk (12 mm diameter, 3 mm thickness) of 0.17 MPa, which is well within the recommended operating range for these stationary phases (<5 MPa).

The average axial pore velocity was calculated as the mean of the z-components (u_z) of pore velocities over the entire pore volume,

$$u_z^{\text{avg}} = \frac{\sum_{i=1}^{N_V} (u_z)_i}{N_V} \tag{6}$$

Here $i = 1 \ldots N_V$ indexes the array of void (pore) voxels throughout the volume, where N_V is the total number of void voxels in the structure. The average velocity calculated in this manner was 0.00195 m/s.

The permeability, as defined by Eq. (1), was calculated as 1.95×10^{-14} m^2. This is within the range of experimental values of 0.63×10^{-14} [18], 1.1×10^{-14} m^2 [27] and 3.0×10^{-14} m^2 [8] reported in studies using CIM disks. These significantly different values suggest physical variability of material properties from one polymer disk to another and it is conceivable that the isolated structure of the specific sample block used for the simulations could exhibit a permeability value lower or higher than the global average.

The Reynolds number,

$$Re = \frac{u_z^{\text{avg}} \cdot d_e}{\nu} \tag{7}$$

is a convenient indicator of the flow regime. Here ν is the kinematic viscosity and d_e the characteristic length, or equivalent particle diameter. Specification of the equivalent diameter is not an easy task since the irregular structure of the polymer monoliths does not yield an obvious length scale based on simple geometric considerations. For this reason, the approach proposed by Leinweber et al. [29] has been adopted, where the equivalent diameter is defined as a hydraulic length related to the permeability, κ. By using the permeability relation in the Kozeny–Carman equation relative to Eq. (1), the characteristic length becomes

$$d_e = \sqrt{\frac{150 \cdot (1-\varepsilon)^2}{\varepsilon^3} \cdot \kappa} \tag{8}$$

where ε is the porosity of the monolith. For the porosity and permeability values reported above, the characteristic length for the monolith sample in this study is thus calculated as 1.9 μm, and the global Reynolds number for the average velocity is then 0.0037. The maximum axial velocity among all sections is 0.0225 m/s, which gives a Reynolds number of 0.057. Thus even taking into account the highest velocities, creeping flow can be assumed at all pore locations.

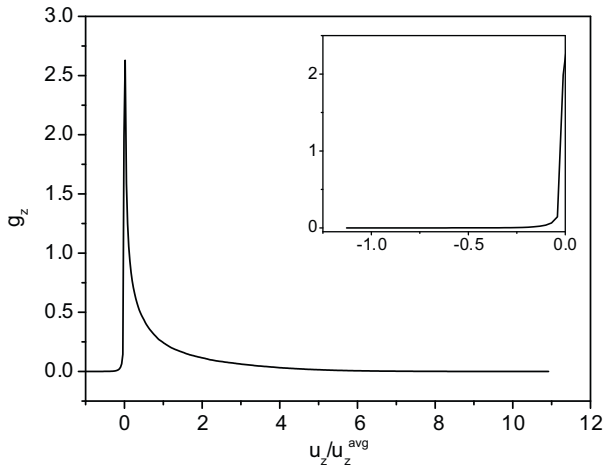

Fig. 6. Normalized histogram of the axial velocities of the calculated flow field. Inset displays the lower tail of the distribution on an expanded scale for clarity.

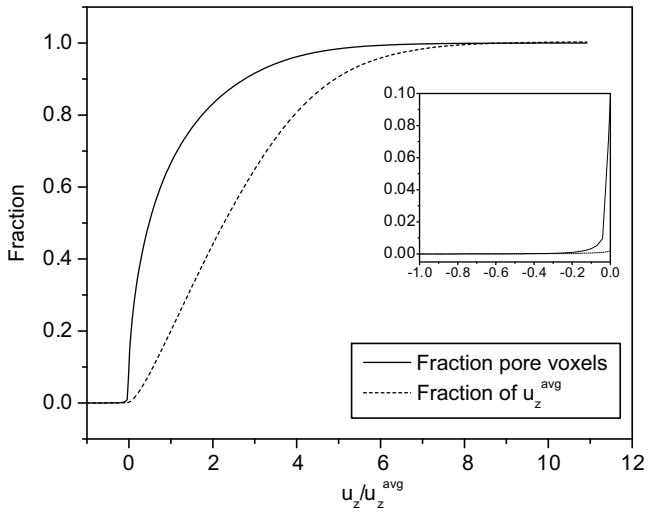

Fig. 7. Cumulative plots of the fraction of pore voxels and the average velocity as a function of scaled axial velocity.

3.3.2. Velocity distribution

The axial velocity distribution function is simply a histogram of the z-velocity values, scaled by the average and normalized to yield an integral of unity, i.e.,

$$g_z\left(\frac{u_z}{u_z^{\mathrm{avg}}}\right) = \frac{G_z(u_z/u_z^{\mathrm{avg}})}{\int_{-\infty}^{\infty} G_z(u_z/u_z^{\mathrm{avg}}) \cdot d(u_z/u_z^{\mathrm{avg}})} \tag{9}$$

where G and g designate the frequency distribution before and after normalization, respectively. Distributions for the lateral velocities (i.e. g_x and g_y) were obtained by applying the same procedure to the respective velocity component for all pore voxels.

The axial velocity distribution function is shown in Fig. 6, where the inset displays the lower velocities on an expanded scale. The distribution ranges from a negative lower limit with magnitude of about 1.0 u_z^{avg} and extends to a maximum of 11.5 u_z^{avg}, that is, from −0.00195 m/s to 0.0225 m/s. A detailed discussion of the negative velocities is deferred to the next section but it is clear from the inset that they are significant both in magnitude and frequency.

Overall, the axial velocity distribution function exhibits a sharp, narrow peak near zero and a rapidly decaying tail, which suggests that the volumetric flow is not distributed evenly throughout the volume, most of it being carried by the higher velocity elements that form a relatively small fraction of the total pore voxels. This skewed behavior is quantitatively illustrated in Fig. 7, where two cumulative functions are displayed as a function of the normalized velocities: the fraction of pore voxels that comprise velocities of the corresponding abscissa value or lower, and the fraction of the integral that these voxels constitute in the calculation of the first moment (i.e., the average velocity). For example, it can be seen from the graph that about two-thirds of all velocities are less than or equal to the average (the continuous curve), yet these account for only 20% of the first moment integral (the dashed curve).

The lateral velocities, on the other hand, display no such skew and are completely symmetric around zero as illustrated in Fig. 8 for the x-component. The y-component histogram, not shown here, is almost identical to that in Fig. 8, similar to what has been observed by Hlushkou et al. [70] for silica monoliths.

3.3.3. Localization of point velocities

While the histograms displayed above provide insight into the quantitative global features of the flow field, they do not convey the important details of the interaction of flow and geometry. To this end, localized magnitude plots of the velocities within regions of interest are helpful in visualizing the flow, and in particular the clustering of the high and low magnitude velocities with respect to the geometry. Fig. 9a displays the normalized axial velocity field for section 250 (at z = 9.6 μm), color-coded with respect to magnitude and overlaid on top of the two-dimensional solid geometry (in black), while Fig. 9b shows a height-map of the same section.

These images confirm that throughout the section there exist hot-spots of 5–6 times the average velocity, surrounded by low-velocity regions. This trend is observed in virtually all of the other sections as well, which raises the question of whether these high-velocity clusters are connected, i.e., if they are effectively part of preferential flow paths. To assess this possibility, it is useful to examine the full three-dimensional map of the magnitude of the total velocity, which allows visualization of both axial and lateral channels of significance. Fig. 10 shows such a plot for a selected portion of the sample block, specifically between z-positions 3.7 and 5.5 μm. The plot shows that the high intensity velocities cluster in three dimensions and extend significantly along the axial direction. Analysis of longer z-distances indicates that these high-velocity regions are interconnected to span the entire length of the sample block.

It is also worth noting from Fig. 10 that the high-velocity clusters are not confined to the central region, where the effects of mirroring on the pore size distribution are the most significant,

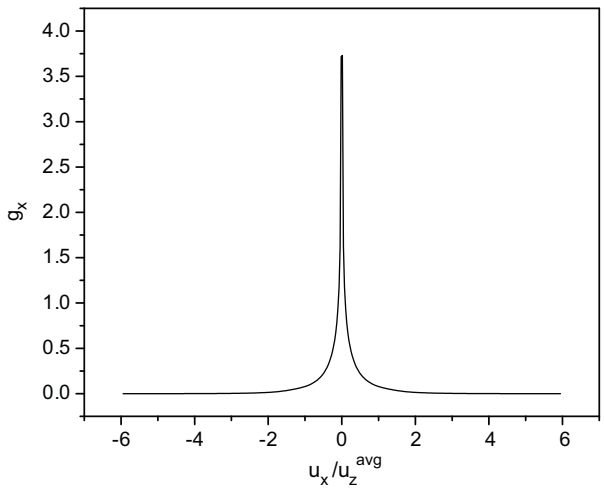

Fig. 8. Normalized histogram of the scaled x-velocities of the flow field.

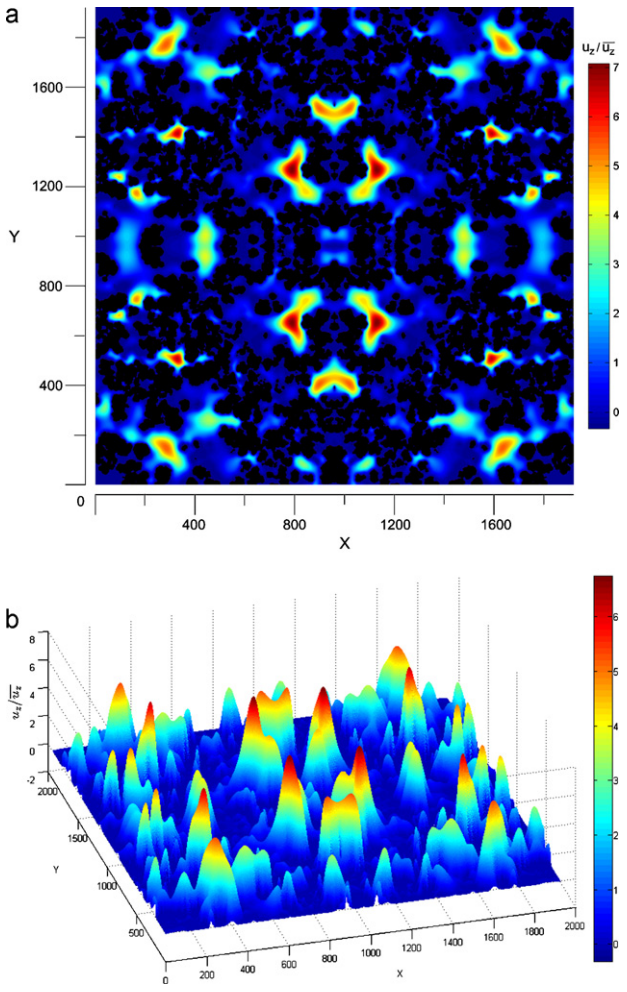

Fig. 9. (a) Color map of axial velocity in one entire section (i.e., *xy* plane) of the block. u_z is normalized by the average axial velocity. The solid geometry is shown in black. (b) Height map of normalized axial velocities in the same section. The *X* and *Y* values are position values in pixels.

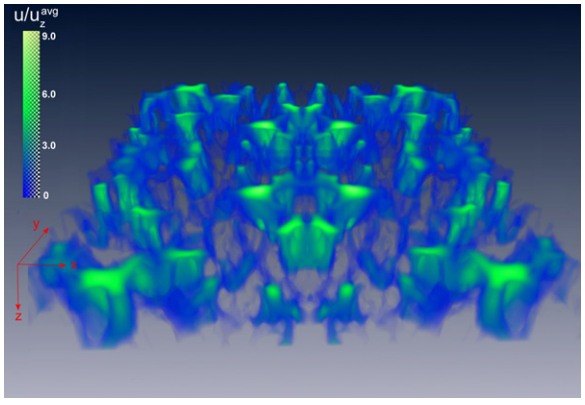

Fig. 10. Plot of *u* (total velocity) values in a 3D segment of the flow field, from $z = 3.7$ to 5.5 μm (sections 200–300). The values are coded by a combined gradient of color and transparency, with the velocities displayed as opaque green at their highest, a translucent mixture of green and blue at mid-range, and completely transparent, therefore invisible at solid voxels where the total vector is zero. (For interpretation of the references to color in this figure legend, the reader is referred to the web version of this article.)

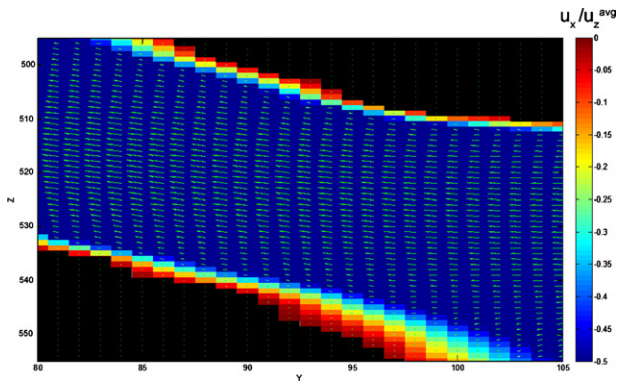

Fig. 11. Two-dimensional vector plot of *y*-and *z*-velocities in a region with significant negative u_z values (sections 480–560, $z = 8.8$–10.4 μm). The *x*-components of the flow are perpendicular to the depicted plane and their magnitudes are color-coded. The solid (i.e. pore walls) is shown in black. The arrow size represents the relative magnitudes of u_z and u_y but the color of the arrows is not related to the color map. Position (*Y* and *Z*) values indicate pixels.

as mentioned previously. The preferential flow appears to be randomly distributed throughout the geometry.

The negative axial velocities, mentioned previously, have magnitudes up to u_z^{avg} and a frequency of almost 10 percent of all velocities (see inset of Fig. 7), so these are quite significant and not computational artifacts. Occurrences of counter-current flow components in the laminar regime of complex porous media are experimentally well documented [47,91,92] and predicted by simulations [62,66,70].

To investigate the nature of the negative u_z components of the flow field obtained in this study, the region with the strongest negative velocities was isolated. Fig. 11 shows vector plots of the *y*- and *z*- components of the local velocities in a *yz* cross-section of this region. In this figure, the axial dimension *z* is depicted as the vertical axis per the convention in previous figures, and *y* as the horizontal. The components in the third dimension *x* are perpendicular to the page and their magnitudes are color-coded. It is apparent from this figure that the geometry in this region consists of a pore that is mainly horizontal (i.e., extends perpendicular to the flow direction), with a slight vertical slope. The flow field simply conforms to this topography, as a primarily lateral flow with a small but distinct vertical component in the direction of decreasing *z*, hence exhibiting the negative axial velocities. Thus in this case at least, complex transition phenomena such as stationary eddies and short-range recirculation can be ruled out, as would be expected in creeping flow.

3.3.4. Comparison with flow fields in other geometries

It is useful to compare the computed velocity distribution for the CIM monolith with other examples of flow in porous media in the literature, in particular to shed light on the apparent imbalance in the distribution of flow. Such biased velocity fields have been observed in simulations of sphere packs, specifically in ordered packs or random-pack arrays with artificially placed defects [59,62,63]. In such geometries, slow zones dominate throughout, forming the narrow peak of the distribution, whereas faster regions occur with much lower frequency but carry the bulk of the flow. Fig. 12 displays a comparison of the CIM monolith flow field obtained in this study with distributions in three other structures: a BCC (body-centered cubic) ordered sphere pack [62], a defective random sphere pack where sphere clusters were extracted to generate a continuous wide-pore channel spanning the entire flow length [63] and a regular random sphere pack [62]. It can be seen that the CIM flow field resembles the BCC pack and the defective random pack distributions closely in shape, all of

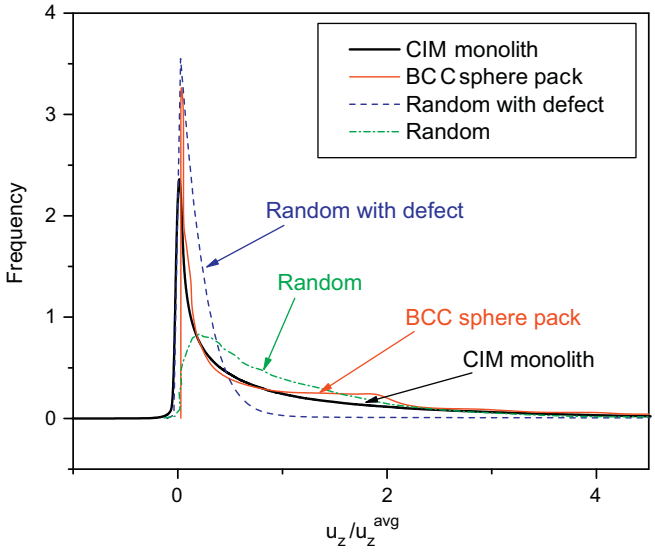

Fig. 12. Comparison of the monolith flow field obtained in this study to sphere-pack solutions of a regular random pack [62], a defective random pack [63] and a BCC ordered pack [62].

them displaying a sharp, narrow peak near zero velocity, due to heterogeneity in their corresponding flow fields.

The flow field in a CapRod silica monolith sample, obtained recently by Hlushkou et al. [70], provides another excellent case for comparison. Fig. 13 displays the two distributions. To compare the two distributions on an equal basis, the velocities for the silica monolith were scaled by the superficial velocity and porosity values of 0.0032 m/s and 0.7, respectively, while the frequency values were normalized by the total integral as indicated by Eq. (9). It can be observed that the silica sample has a wider, lower peak around zero and comparatively fewer negative velocities. It is possible that the relatively regular geometry of the silica monoliths, where the flow-through pores have a much narrower distribution, combined with the larger porosity (0.7 as opposed to 0.55 for the polymer monolith), results in a more evenly distributed flow field compared to the heterogeneous polymeric monolith structure with a broad distribution of pores that can accommodate varying degrees of convective flow.

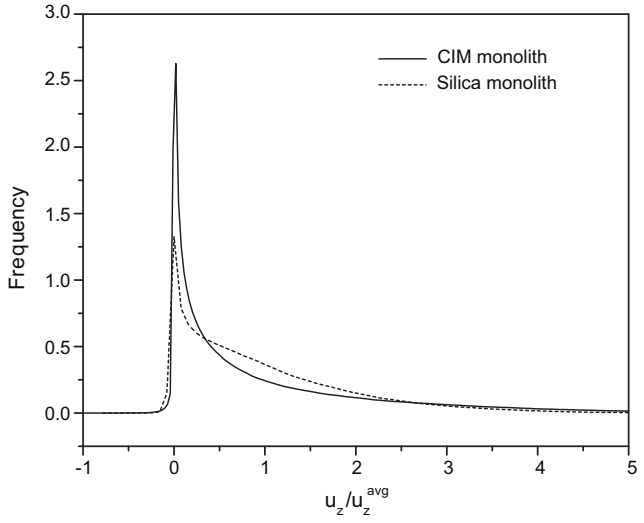

Fig. 13. Comparison of the monolith flow field obtained in this study (continuous curve) with the flow field obtained for a silica monolith sample (dashed curve) [70].

4. Conclusions

We have calculated the velocity distribution for a sample block of a polymeric monolith using LB methods. The calculated permeability value is within the range of reported experimental values, which is a satisfactory result, considering the heterogeneity of these materials. The flow field is skewed towards lower velocities, and shows evidence of uneven distribution of local flow.

Assuming that the flow field obtained here is an accurate representation of actual monolith behavior, these results can be interpreted for qualitative insight on mass transfer performance as well. In particular, complex behavior due to competing influences may be expected. On the one hand, the absence of an intraparticle diffusional resistance will reduce diffusive limitations encountered in beds of porous particles, but on the other hand, the extensive heterogeneity of flow due to the influence of factors such as the presence of preferential flow paths, lateral and countercurrent displacement and stagnant zones will increase dispersion. For instance, as mentioned previously, the histogram of the local velocities in this study bears a significant resemblance to that of a defective sphere pack with a wide channel. Dispersion simulations [59] have shown that such defects give rise to fast flow paths and correspondingly re-define the length and time scales for dispersion. This in turn induces non-asymptotic dispersion behavior due to the increased time needed for solutes to laterally sample the preferential flow path(s), which are sparse and control the flow [59]. Similar effects have been reported for simulations of sphere packs with varying levels of non-uniformity, where local, microscopic packing disorders have been shown to influence dispersion behavior significantly [67].

Since we have solved the flow equations for a direct reconstruction of a physical sample without introduction of adjustable or estimated parameters, whether these results accurately reflect actual detailed flow behavior depends mostly on how representative the sample is of an entire monolith disk. Wall effects, which have been shown to cause significant distortion in the velocity field and dispersion in packed beds [59,68,93] as well as in silica monoliths [71,94], have been neglected in this study. The computed velocity distribution should thus be representative of the monolith core and the remaining issue then is whether the size of the sample is large enough to capture all macroscopic phenomena that occur in this region. In the absence of complete velocity fields obtained through direct imaging, this is difficult to ascertain. However, the developed method is sufficiently robust to extend and expand to larger sample sizes or to additional samples to confirm reproducibility.

Acknowledgements

We thank Paul Miller and Christel Genoud of Gatan Inc. for the serial-sectioning and imaging of our sample with the 3-View system, and Dr. Ulrich Tallarek for providing detailed results of simulations on silica monoliths. Financial support for this work was provided by the National Institutes of Health (NIH) under grant R01 GM75047.

References

[1] G. Carta, A.R. Ubiera, T.M. Pabst, Chem. Eng. Technol. 28 (2005) 1252.
[2] A.K. Hunter, G. Carta, J. Chromatogr. A 971 (2002) 105.
[3] A. Nir, L.M. Pismen, Chem. Eng. Sci. 32 (1977) 35.
[4] A.E. Rodrigues, B.J. Ahn, A. Zoulalian, AIChE J. 28 (1982) 541.
[5] D.D. Frey, E. Schweinheim, C. Horvath, Biotechnol. Prog. 9 (1993) 273.
[6] G. Guiochon, J. Chromatogr. A 1168 (2007) 101.
[7] A. Jungbauer, R. Hahn, J. Chromatogr. A 1184 (2008) 62.
[8] F. Svec, T.B. Tennikova, Z. Deyl (Eds.), Monolithic Materials: Preparation, Properties and Applications, Elsevier, Amsterdam, 2003.
[9] M.R. Buchmeiser, Polymer 48 (2007) 2187.

[10] H. Minakuchi, K. Nakanishi, N. Soga, N. Ishizuka, N. Tanaka, Anal. Chem. 68 (1996) 3498.
[11] K. Nakanishi, N. Soga, J. Am. Ceram. Soc. 74 (1991) 2518.
[12] S. Hjertén, J.-L. Liao, R. Zhang, J. Chromatogr. A 473 (1989) 273.
[13] T.B. Tennikova, M. Bleha, F. Svec, T.V. Almazova, B.G. Belenkii, J. Chromatogr. A 555 (1991) 97.
[14] K. Nakanishi, H. Minakuchi, N. Soga, N. Tanaka, J. Sol–Gel Sci. Technol. 8 (1997) 547.
[15] M. Al-Bokari, D. Cherrak, G. Guiochon, J. Chromatogr. A 975 (2002) 275.
[16] D. Moravcova, P. Jandera, J. Urban, J. Planeta, J. Sep. Sci. 27 (2004) 789.
[17] F. Svec, J. Chromatogr. A 1217 (2010) 902.
[18] E.I. Trilisky, H. Koku, K.J. Czymmek, A.M. Lenhoff, J. Chromatogr. A 1216 (2009) 6365.
[19] J. Courtois, M. Szumski, F. Georgsson, K. Irgum, Anal. Chem. 79 (2007) 335.
[20] J.-L. Cabral, D. Bandilla, C.D. Skinner, J. Chromatogr. A 1108 (2006) 83.
[21] R. Hahn, M. Panzer, E. Hansen, J. Mollerup, A. Jungbauer, Sep. Sci. Technol. 37 (2002) 1545.
[22] S.L. Williams, M.E. Eccleston, N.K.H. Slater, Biotechnol. Bioeng. 89 (2005) 783.
[23] P. Kramberger, M. Peterka, J. Boben, M. Ravnikar, A. Strancar, J. Chromatogr. A 1144 (2007) 143.
[24] P. Kramberger, R.C. Honour, R.E. Herman, F. Smrekar, M. Peterka, J. Virol. Methods 166 (2010) 60.
[25] A. Zochling, R. Hahn, K. Ahrer, J. Urthaler, A. Jungbauer, J. Sep. Sci. 27 (2004) 819.
[26] M.K. Danquah, G.M. Forde, J. Chem. Technol. Biotechnol. 82 (2007) 752.
[27] I. Mihelic, D. Nemec, A. Podgornik, T. Koloini, J. Chromatogr. A 1065 (2005) 59.
[28] U. Tallarek, F.C. Leinweber, A. Seidel-Morgenstern, Chem. Eng. Technol. 25 (2002) 1177.
[29] F.C. Leinweber, D. Lubda, K. Cabrera, U. Tallarek, Anal. Chem. 74 (2002) 2470.
[30] H. Oberacher, A. Premstaller, C.G. Huber, J. Chromatogr. 1030 (2004) 201.
[31] F.C. Leinweber, U. Tallarek, J. Chromatogr. A 1006 (2003) 207.
[32] C. Horvath, H.-J. Lin, J. Chromatogr. 126 (1976) 401.
[33] J.K. Knox, J. Chromatogr. Sci. 15 (1977) 352.
[34] J.J. van Deemter, F.J. Zuiderweg, A. Klinkenberg, Chem. Eng. Sci. 5 (1956) 271.
[35] J.C. Giddings, Dynamics of Chromatography, Marcel Dekker, New York, 1965.
[36] H. Minakuchi, N. Ishizuka, K. Nakanishi, N. Soga, N. Tanaka, J. Chromatogr. A 828 (1998) 83.
[37] H. Minakuchi, K. Nakanishi, N. Soga, N. Ishizuka, N. Tanaka, J. Chromatogr. A 762 (1997) 135.
[38] H. Minakuchi, K. Nakanishi, N. Soga, N. Ishizuka, N. Tanaka, J. Chromatogr. A 797 (1998) 121.
[39] F. Gritti, W. Piatkowski, G. Guiochon, J. Chromatogr. A 983 (2003) 51.
[40] M. Kele, G. Guiochon, J. Chromatogr. A 960 (2002) 19.
[41] K. Miyabe, A. Cavazzini, F. Gritti, M. Kele, G. Guiochon, Anal. Chem. 75 (2003) 6975.
[42] R. Hahn, A. Jungbauer, Anal. Chem. 72 (2000) 4853.
[43] A. Jungbauer, J. Chromatogr. A 1065 (2005) 3.
[44] R. Hahn, A. Tscheliessnig, P. Bauerhansl, A. Jungbauer, J. Biochem. Biophys. Methods 70 (2007) 87.
[45] K.E. Thompson, H.S. Fogler, AIChE J. 43 (1997) 1377.
[46] K.R. Westerterp, R.J. Wijngaarden, N.B.G. Nijhuis, Chem. Eng. Technol. 19 (1996) 291.
[47] A.J. Sederman, M.L. Johns, P. Alexander, L.F. Gladden, Chem. Eng. Sci. 53 (1998) 2117.
[48] N. Vervoort, H. Saito, K. Nakanishi, G. Desmet, Anal. Chem. 77 (2005) 3986.
[49] J.J. Meyers, A.I. Liapis, J. Chromatogr. A 852 (1999) 3.
[50] A.I. Liapis, J.J. Meyers, O.K. Crosser, J. Chromatogr. A 865 (1999) 13.
[51] K. Miyabe, G. Guiochon, J. Phys. Chem. B 106 (2002) 8898.
[52] J. Billen, P. Gzil, G.V. Baron, G. Desmet, J. Chromatogr. A 1077 (2005) 28.
[53] N. Vervoort, P. Gzil, G.V. Baron, G. Desmet, Anal. Chem. 75 (2003) 843.
[54] N. Vervoort, P. Gzil, G.V. Baron, G. Desmet, J. Chromatogr. A 1030 (2004) 177.
[55] J. Salles, J.F. Thovert, R. Delannay, L. Prevors, J.L. Auriault, P.M. Adler, Phys. Fluids A 5 (1993) 2348.
[56] R.S. Maier, D.M. Kroll, H.T. Davis, R.S. Bernard, Internat. J. Modern Phys. C 9 (1998) 1523.
[57] R.S. Maier, D.M. Kroll, R.S. Bernard, S.E. Howington, J.F. Peters, H.T. Davis, Phys. Fluids 12 (2000) 2065.
[58] R.S. Maier, D.M. Kroll, R.S. Bernard, S.E. Howington, J.F. Peters, H.T. Davis, Phil. Trans. R. Soc. A 360 (2002) 497.
[59] R.S. Maier, M.R. Schure, J.P. Gage, J.D. Seymour, Water Resour. Res 44 (2008) S03, W06.
[60] R.S. Maier, R.S. Bernard, J. Comput. Phys. 229 (2010) 233.
[61] M.R. Schure, R.S. Maier, D.M. Kroll, H.T. Davis, Anal. Chem. 74 (2002) 6006.
[62] M.R. Schure, R.S. Maier, D.M. Kroll, H.T. Davis, J. Chromatogr. A 1031 (2004) 79.
[63] M.R. Schure, R.S. Maier, J. Chromatogr. A 1126 (2006) 58.
[64] D. Kandhai, D. Hlushkou, A.G. Hoekstra, P.M.A. Sloot, H. Van As, U. Tallarek, Phys. Rev. Lett. 88 (2002) 234501.
[65] D. Kandhai, U. Tallarek, D. Hlushkou, A. Hoekstra, P.M.A. Sloot, H. Van As, Philos. Trans. R. Soc. A: Math. Phys. Eng. Sci. 360 (2002) 521.
[66] R.S. Maier, D.M. Kroll, Y.E. Kutsovsky, H.T. Davis, R.S. Bernard, Phys. Fluids 10 (1998) 60.
[67] S. Khirevich, A. Daneyko, A. Höltzel, A. Seidel-Morgenstern, U. Tallarek, J. Chromatogr. A 1217 (2010) 4713.
[68] S. Khirevich, A. Holtzel, D. Hlushkou, U. Tallarek, Anal. Chem. 79 (2007) 9340.
[69] S. Khirevich, A. Holtzel, A. Seidel-Morgenstern, U. Tallarek, Anal. Chem. 81 (2009) 7057.
[70] D. Hlushkou, S. Bruns, U. Tallarek, J. Chromatogr. A 1217 (2010) 3674.
[71] D. Hlushkou, S. Bruns, A. Holtzel, U. Tallarek, Anal. Chem. 82 (2010) 7150.
[72] G.R. McNamara, G. Zanetti, Phys. Rev. Lett. 61 (1988) 2332.
[73] S. Chen, G.D. Doolen, Annu. Rev. Fluid Mech. 30 (1998) 329.
[74] S. Succi, The Lattice Boltzmann Equation for Fluid Dynamics and Beyond, Oxford University Press, New York, 2001.
[75] C. Manwart, U. Aaltosalmi, A. Koponen, R. Hilfer, J. Timonen, Phys. Rev. E: Stat. Nonlinear Soft Matter Phys. 66 (2002) 016702.
[76] J. Bernsdorf, G. Brenner, F. Durst, Comput. Phys. Commun. 129 (2000) 247.
[77] M.E. Kutay, A.H. Aydilek, E. Masad, Comput. Geotechnol. 33 (2006) 381.
[78] B. Manz, L.F. Gladden, P.B. Warren, AIChE J. 45 (1999) 1845.
[79] M.A. Hayat, Principles and Techniques of Electron Microscopy: biological applications, 3rd ed., CRC Press, Boca Raton, FL, 1989.
[80] W. Denk, H. Horstmann, PLoS Biol. 2 (2004) e329.
[81] P. Perona, J. Malik, IEEE Trans. Pattern Anal. Machine Intell. 12 (1990) 629.
[82] N. Otsu, IEEE Trans. Syst. Man Cybern SMC-9 (1979) 62.
[83] J. Serra, Image Analysis and Mathematical Morphology, Academic Press, London, 1982.
[84] Y. Yao, A.M. Lenhoff, J. Chromatogr. A 1126 (2006) 107.
[85] H.J. Vogel, K. Roth, Adv. Water Resour. 24 (2001) 233.
[86] X. He, L.-S. Luo, Phys. Rev. E: Stat. Nonlinear, Soft Matter Phys. 55 (1997) R6333.
[87] R.S. Maier, R.S. Bernard, D.W. Grunau, Phys. Fluids 8 (1996) 1788.
[88] W. Gropp, E. Lusk, A. Skjellum, Using MPI: Portable Parallel Programming with the Message-Passing Interface, 2nd ed., MIT Press, Cambridge, MA, 1999.
[89] E.C. Peters, F. Svec, J.M.J. Frechet, Chem. Mater. 9 (1997) 1898.
[90] F. Svec, J.M.J. Frechet, Ind. Eng. Chem. Res. 38 (1999) 34.
[91] A.J. Sederman, M.L. Johns, A.S. Bramley, P. Alexander, L.F. Gladden, Chem. Eng. Sci. 52 (1997) 2239.
[92] Y.E. Kutsovsky, L.E. Scriven, H.T. Davis, B.E. Hammer, Phys. Fluids 8 (1996) 863.
[93] R.S. Maier, D.M. Kroll, R.S. Bernard, S.E. Howington, J.F. Peters, H.T. Davis, Phys. Fluids 15 (2003) 3795.
[94] K.S. Mriziq, J.A. Abia, Y. Lee, G. Guiochon, J. Chromatogr. A 1193 (2008) 97.